




Merits of photocatalytic activity of synthesized $(\text{Zn}_x\text{Cu}_{(1-x)}\text{Fe}_2\text{O}_4)$; $x = (0-1)$ magnetic nanoparticles for wastewater treatment

Osama H. Abuzeayad^{1,*}, Ahmed M. El-Khawaga^{2,*} , Mohamed A. Elsayed¹, Mohamed Gobara¹, and Hesham Tantawy¹

¹ Department of Chemical Engineering, Military Technical College (MTC), Cairo, Egypt

² Department of Basic Medical Sciences, Faculty of Medicine, Galala University, Galala City, Suez 43511, Egypt

Received: 27 September 2023

Accepted: 3 February 2024

Published online:

4 March 2024

© The Author(s), 2024

ABSTRACT

Synthesis of crystalline zinc copper ferrite nanoparticles was achieved via a simple co-precipitation method. Scanning electron microscope (SEM) is utilized to give the morphological characterization of the prepared samples. A transmission electron microscope (TEM) was employed for further identification and confirmation of the particle size and morphology. Moreover, X-ray diffraction (XRD) and Fourier transformation infrared (FTIR) spectroscopy were utilized to examine crystalline structure and chemical structure, respectively. The photocatalytic performance of $\text{Zn}_{0.5}\text{Cu}_{0.5}\text{Fe}_2\text{O}_4$ nanoparticles under UV light was assessed by decolorization of methyl orange (MO) azo dye. The efficiency of photocatalytic degradation of 20 ppm of MO by $\text{Zn}_{0.5}\text{Cu}_{0.5}\text{Fe}_2\text{O}_4$ nanoparticles 15 mg was 96% after 135 min at an ambient temperature of 25 °C and pH value of 3. Further interpretation was carried out and a proposed mechanism for the MO photodegradation over $\text{Zn}_{0.5}\text{Cu}_{0.5}\text{Fe}_2\text{O}_4$ nanoparticles was suggested.

Introduction

Ferrites are a large class of oxides that have magnetic characteristics [1], and the most prevalent kind of magnetic ferrite is cubic spinel with M ferrite [2]. Spinel M ferrite in nanoparticle form is a beneficial class of magnetic nanomaterials for its special magnetic, electrical, and catalytic capabilities, and is consequently used in numerous scientific and industrial fields [3], including photocatalytic activity [4], ferrofluid technology,

sensors technology, clinical diagnostics, high-density data storage, drug delivery, electrical devices, catalysts, and high power microwave applications. Their synthesis is made up of simple, inexpensive approaches that make up its advantageous position in mass production processes [5, 6].

Up to now many methods used for the preparation of magnetic metal ferrite nanoparticles such as co-precipitation [7, 8], mechanochemical [9], hydrothermal/solvothermal [10], and sol-gel approaches [11]. The

Handling Editor: Dale Huber.

Address correspondence to E-mail: abuzeyadosama@gmail.com; Ahmed.ElKhawaga@gu.edu.eg

co-precipitation method is the most famous method for the preparation of ferrites [12], as it has the benefits of simple preparation, uncomplicated [4], inexpensive and gentle chemistry route that produces an ultra-fine and homogeneous powder [13].

On the other hand, the textile, printing, and dyeing industries are the industries of huge water consumption with the annual wastewater discharge accounting for about 70% of the world's total discharge azo dyes with stable azo functional groups (N=N) and aromatic rings are difficult to be biodegraded, and have strong chromaticity and toxicity, which pose a serious threat to the environment, aquatic organisms and human life. MO is a member of the azo dyes family and is an organic substance that is known to be carcinogenic and mutagenic. Magnetic nanocomposites are promising new materials for the photodegradation of organic contaminants. They have several advantages over commercial TiO₂, including a narrow band gap, high surface area, magnetic properties, and stability [14]. These advantages make these magnetic nanocomposites more efficient, reliable, and cost-effective for real-world applications.

In this work, the synthesis of Zn_xCu_(1-x)Fe₂O₄ nanoparticles was carried out by the co-precipitation process to examine their structural, optical properties, and photodegradation efficiency of methyl orange (MO).

Materials and methods

Chemicals

Fe₂(SO₄)₃·5H₂O, Cu(SO₄)·6H₂O, Zn(SO₄)·7H₂O, sodium hydroxide (NaOH), and methyl orange (MO) were acquired from E-Merck Products. The remaining reagents have a purity equivalent to analytical grade and without any further purification before use.

Synthesis of Zn_xCu_(1-x)Fe₂O₄

The co-precipitation approach was used to produce Zn Cu Ferrite (Zn_xCu_(1-x)Fe₂O₄) nanoparticles made up of compositions ($x = 0, 0.2, 0.5, 0.8, 1.0$). Fe₂(SO₄)₃·5H₂O, Cu(SO₄)·6H₂O, Zn(SO₄)·7H₂O were utilized in stoichiometric amounts from pure raw materials to produce the necessary solutions with the essential molarities. The solution of Fe₂(SO₄)₃·5H₂O, 0.4 M (25 ml), and different content of Cu(SO₄)·6H₂O and Zn(SO₄)·7H₂O were first mixed for 30 min then suddenly added to 1 M hot NaOH solution 80–90 °C under stirring of 1500 rpm. The obtained colloidal solution of pH 11–13

was kept at 80–90 °C for 1 h. Then it was left to cool down till the precipitate settled down. The clear solution was removed carefully without losing the precipitate. This process was repeated with hot deionized water until the filtrate had a pH of 7, 10 times to ensure the removal of Na₂SO₄ and excess of NaOH from the solution [15]. Then the samples were washed with Acetone and dried at room temperature for 72 h as shown in Fig. 1.

Characterization of the Zn_xCu_(1-x)Fe₂O₄ nanoparticles

Different characterization methods were used for identifying the synthesized Zn_xCu_(1-x)Fe₂O₄ nanoparticles. X-ray diffractometer type (X'Pert PRO) Cu K α radiation ($\lambda = 1.5418\text{\AA}$) was used to determine and analyze the phase present in the Cu Zn ferrite nanopowders. FTIR analysis was performed using an FT/IR 4700 spectrometer (Jasco, Tokyo, Japan). The specimens were produced using potassium bromide (KBr) pellets. The FTIR spectra were obtained within the frequency range of 400–4000 cm⁻¹, with a resolution of 4 cm⁻¹ and an average of 32 scans. Scanning electron microscope (SEM) type FEI Czech at KV 25–30 kV, magnification 150X, and an average working distance of 15 mm was employed for morphological and semi-quantitative elemental analysis. High-Resolution Transmission Electron Microscope (HRTEM)—model JEM-2100, JEOL, Japan, was also used for detailed morphological characterization. Agilent Cary 60 UV–Vis spectrophotometer was operated to examine the UV–Vis spectrum.

Photocatalytic reactor

Photocatalytic degradation of the (MO) was attained through the use of a UV lamp and a catalyst called Zn_xCu_(1-x)Fe₂O₄. The UV reactor in use had a glass cylinder shape (100 ml), measuring 3 cm in diameter by 27 cm in length, as shown in Fig. 2, and was covered in a thin layer of aluminum foil. 50 ml of contaminated solutions filled the photoreactor.

The UV light irradiation source was a commercial UV-C Lamp, PHILIPS TUV 11WG11 T5; it's a high-pressure mercury lamp 11 W and has a mean wavelength 254 nm. It is immersed in the contaminated solutions, while the photoreactor is kept at about 25 °C by a water bath.

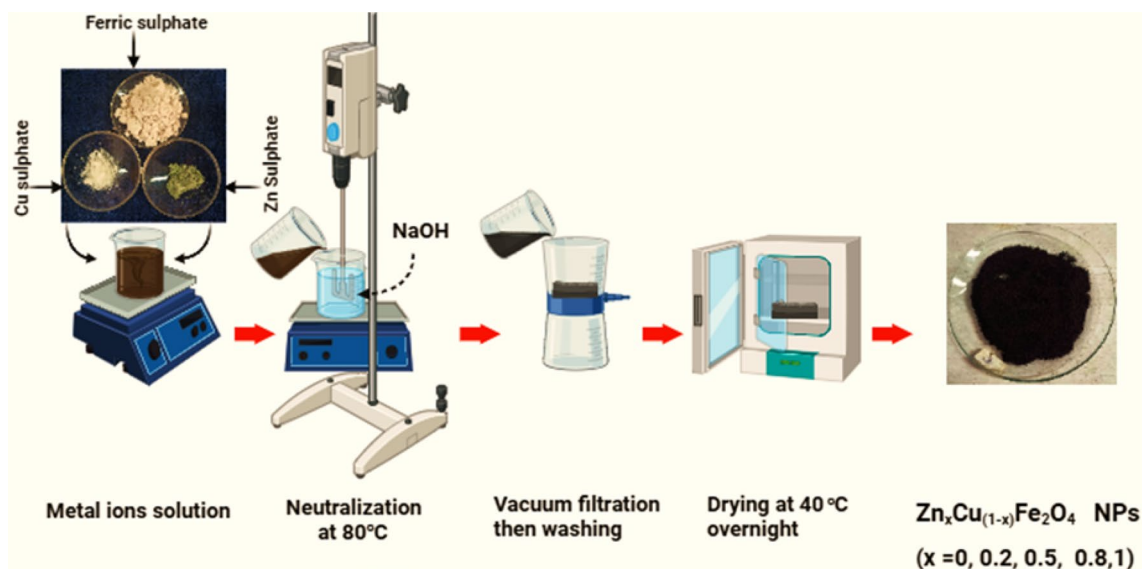


Figure 1 Schematic figure of $Zn_xCu_{(1-x)}Fe_2O_4$ nanoparticles preparation.

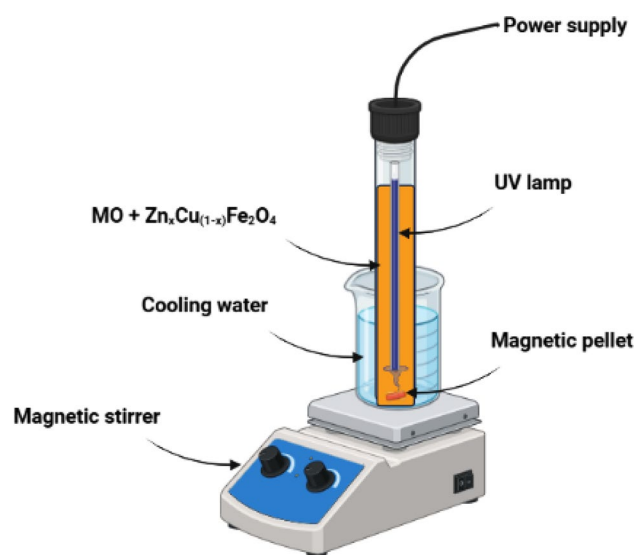


Figure 2 Using the photochemical cell in the photocatalytic process.

A nanocomposite weighing 10 mg was introduced into a 50 ml aqueous solution containing methyl orange (MO) with an initial concentration (C_0) of 10 mg/L. The mixture was stirred continuously at room temperature (25 °C) for 135 min in the absence of light to establish equilibrium between the adsorption and desorption processes. On the other hand, a simulated UV light source was employed to illuminate the solution containing MO dye without the photocatalyst to determine the photolysis of MO dye.

After that, the pollutant (MO) dye and catalyst $Zn_xCu_{(1-x)}Fe_2O_4$ were introduced into the glass cylindrical

reactor and the UV irradiation, 1 ml suspension of the (MO) solution was sampled using a syringe from the UV reactor at a specific time and centrifuged at 20 min and measured the absorbance with a spectrophotometer at wavelength 464 nm [16]. The photodecomposition efficiency (Removal %) was calculated from the following equation [17]:

$$\text{Removal \%} = 1 - \left(\frac{C_t}{C_0} \right) * 100 \quad (1)$$

where C_0 is the MO's (mg/L) initial concentration and C_t represents the concentration at time (t). The operational parameters of photocatalytic degradation, including different initial concentrations of MO dye (5.0, 10.0, and 15.0 ppm) by varying initial MO concentration while maintaining other reaction conditions with no change, photocatalyst dose (5.0, 10.0, and 15.0 mg) and different pH values (pH 3–9) were investigated.

Results and discussion

Characterization of $Zn_xCu_{(1-x)}Fe_2O_4$ nanoparticles

X-ray diffraction patterns

The XRD information attained for the $Zn_xCu_{(1-x)}Fe_2O_4$ ($x = 0, 0.2, 0.5, 0.8, 1$) nanoparticles prepared via

co-precipitation shows different crystallinity according to their composition as reported in Fig. 3. It was so obvious that the ZnFe_2O_4 and CuFe_2O_4 have lower crystallinity and may be polycrystalline structures. On the other hand, samples having both Cu and Zn are more ordered. The main peaks for ZnFe_2O_4 and CuFe_2O_4 are observed around 2θ values $\sim 21.5^\circ$, 33.5° , 35° , 36.5° , 53.3° , 59° , and 61.2° . In addition to a broad weak peak around $2\theta \sim 40^\circ$ [18]. On the other hand, the $\text{Zn}_x\text{Cu}_{(1-x)}\text{Fe}_2\text{O}_4$ (0.2, 0.5, 0.8) samples shows a relative sharp and clear peaks around 2θ values $\sim 30.1^\circ$, 35.2° , 37.5° , 43.1° , 53.0° , 56.9° , and 62.8° [19]. These results indicate the relative higher crystallinity of $\text{Zn}_x\text{Cu}_{(1-x)}\text{Fe}_2\text{O}_4$ ($x = 0.2, 0.5, 0.8$) to ZnFe_2O_4 and CuFe_2O_4 . Even though all the samples are prepared with the same approach but the relative abundance of metallic species controls and tunes the degree of ordering of the obtained structures. Hence, different relative photocatalytic potentials may be considered. In general, the X-ray diffraction patterns are consistent with the standard JCPDS Card No. 22-1012(22-1042) of the cubic $\text{Zn}_x\text{Cu}_{(1-x)}\text{Fe}_2\text{O}_4$ ferrite phase [19].

The observation of identical XRD patterns for ZnFe_2O_4 and CuFe_2O_4 can be attributed to their shared spinel structure. ZnFe_2O_4 and CuFe_2O_4 are both spinels, which means they share the same crystal structure. In spinels, the metal cations (Zn and Cu in this case) occupy two distinct sites within the crystal lattice, known as the tetrahedral (A) and octahedral (B) sites. Despite the difference in atomic number and size between Zn and Cu, their similar

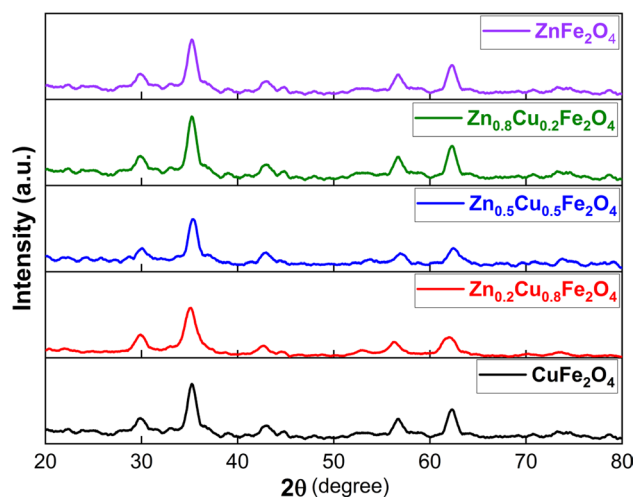


Figure 3 XRD patterns for the synthesized $\text{Zn}_x\text{Cu}_{(1-x)}\text{Fe}_2\text{O}_4$ nanoparticles.

electronic configurations allow them to fit into the same crystal structure, resulting in identical peak positions in the XRD patterns [20]. If the difference in peak positions between ZnFe_2O_4 and CuFe_2O_4 is smaller than the resolution limit of the instrument, the peaks may appear merged, leading to an apparently identical XRD pattern.

Nanoparticle crystallite sizes were calculated utilizing Scherrer's method by evaluating the strongest peak in the X-ray diffraction (XRD) pattern [21]:

$$D = 0.9\lambda / \beta \cos \theta \quad (2)$$

In this context, the symbol λ represents the wavelength of the radiation employed, while β and θ denote the full width at half maximum (FWHM) and the angle corresponding to the peak of highest intensity, respectively. The X-ray diffraction (XRD) analysis revealed that the (311) plane exhibited the highest peak intensity, indicating its prominence in the crystalline structure. According to Scherrer's equation [Eq. 2], the intensity of the cubic spinel ferrite's basic diffraction peak at the (311) plane corresponds to 2θ values $\sim 35.2^\circ$ [18], used as a measurement for the degree of crystallinity [22]. The calculated crystallite size is found to be 47, 42, 38, 32 and 28 nm for $\text{Zn}_x\text{Cu}_{(1-x)}\text{Fe}_2\text{O}_4$ ($x = 0, 0.2, 0.5, 0.8$ and 1.0), respectively. Changing the Zn/Cu ratio in $\text{ZnCuFe}_2\text{O}_4$ can significantly affect the crystal size. Generally, a higher Cu content leads to the formation of larger crystals. This is because Cu ions have a smaller ionic radius (0.72 Å) compared to Zn ions (0.74 Å); this leads to the decrement of densities of nucleation centers of the ferrite sample, which result in the formation of larger crystallite sizes [20, 23, 24].

On the other hand, the relative ratio of Zn and Cu in the prepared samples significantly affects the intensity and crystallinity of its XRD results. This is because the X-ray diffraction pattern is essentially a fingerprint of the crystal structure of the material, and the intensity of the diffracted peaks depends on the relative amounts of the different elements present [25, 26]. As the concentration of Zn increases relative to Cu, the intensity of the peaks corresponding to the Zn-rich phases will increase. Conversely, the intensity of the peaks corresponding to the Cu-rich phases will decrease. This is because the X-rays are more likely to be scattered by the atoms that are present in higher concentrations. The overall background intensity of the XRD pattern may also be affected by the

Zn/Cu ratio [27]. The width of the diffracted peaks can provide information about the crystallinity of the material [28]. Narrow peaks indicate a well-ordered crystal structure, while broad peaks indicate a less ordered structure [29]. In general, as the Zn/Cu ratio increases, the peak width of the Zn-rich phases will decrease, indicating an improvement in crystallinity. This is because the Zn atoms tend to form a more ordered crystal structure than the Cu atoms [30].

Scanning electron microscope (SEM) micrograph of $Zn_xCu_{(1-x)}Fe_2O_4$ nanoparticles

Figure 4 represents the SEM micrograph of the prepared $Zn_xCu_{(1-x)}Fe_2O_4$ nanoparticles. At first glance, the common size was about 30–50 nm. Finer particles are also observed. The larger ones may be aggregates of smaller particles. The impact of changing the composition ratio between copper and zinc is difficult to elaborate clearly. Table 1 lists the elemental analysis (EDX) of the prepared $Zn_xCu_{(1-x)}Fe_2O_4$ nanoparticles.

High-resolution transmission electron microscope (HR-TEM)

To acquire additional facts about the morphology study of the prepared $Zn_xCu_{(1-x)}Fe_2O_4$ nanocatalyst, TEM was employed successfully. As shown in Fig. 5, from the initial glance at all the images, it was obvious large clusters consisted of smaller particles. The observed particle size during the SEM imaging was not representative enough for all the samples. For instance, the $ZnFe_2O_4$ sample showed large size clusters in the SEM image, and the TEM image showed smaller particles. The observed size may be around 30–40 nm. In the same manner, the $CuFe_2O_4$ sample showed a smaller particle size than observed by the SEM. The observed size was about 35–45 nm. Regarding the $Zn_{0.8}Cu_{0.2}Fe_2O_4$ and $Zn_{0.2}Cu_{0.8}Fe_2O_4$ samples showed a broad size distribution around 25–40 nm. Concerning the $Zn_{0.5}Cu_{0.5}Fe_2O_4$ sample, the size could be assumed to be around 38 nm. Finally, the TEM image was more detailed than the SEM. Losing details in the SEM images may be due to the surface charging of samples during interaction with an electron beam [31]. Since all the samples are not conductive and there is no way for charge dissipation and increasing the SEM magnification. In general, the TEM images of each sample indicated the relative abundance

of copper and zinc affects particle size, and morphology and may affect particle crystallinity.

FTIR analysis

Figure 6 displays the results of FTIR spectra of the synthesized $Zn_xCu_{(1-x)}Fe_2O_4$ ferrite nanoparticles that were carried out within a frequency range from 500 to 4000 cm^{-1} . In general, the obtained spectra may be divided into two main regions. The first one represents the fingerprint region (500–1800 cm^{-1}) [32] and the other is the lattice water H–O–H stretching band (3200–3600 cm^{-1}) [33]. Regarding the first region, the identified peaks represent the typical ferros spinel fingerprint features [34]. As a result of the interaction between the oxygen atom and the cations at tetrahedral and octahedral positions, these bands are mostly attributed to the metal–oxygen (M–O) vibration modifications [35]. Tetrahedral group intrinsic vibrations are thought to be responsible for the observed strong transmittance bands about 500 and 700 cm^{-1} [36]. The shift in bond distance M–O in the octahedral and tetrahedral sites may be the cause of the significant variation between these bands among the various samples. The variation in the $M^{n+}-O^{2-}$ distance between the octahedral and tetrahedral compounds is the cause of the difference in band position [37]. The observed transmittance band at 1330 may be assigned to the two metal–oxygen stretching modes $M=O$, those with only one terminal oxygen atom absorb [38]. This band may be related to defect density in the crystal structure, hence propping the photocatalytic potential. The vibrational mode in tetrahedral anions is triply degenerate rather than a simple metal–oxygen stretching frequency, and any minor deviance from tetrahedral symmetry could cause the observed broadbands. Additionally, the bending vibrations of O–H of the adsorbed water molecules from the adsorbing moisture on the surface of the tiny particles are attributed to the peak at 1632 cm^{-1} [39]. The broadband was around 3400 cm^{-1} to the O–H group mode of a stretch of adsorbed hydroxyl group. No more precursor or other impurity-related peaks were noted [40].

The results show that the difference in Zn/Cu ratios significantly affects the FTIR transmittance bands of the prepared samples, primarily due to changes in the vibrational frequencies and electronic structure. Zn and Cu atoms have different masses and electronegativities [25]. When they substitute for each other in a material, the vibrational frequencies of the bonds

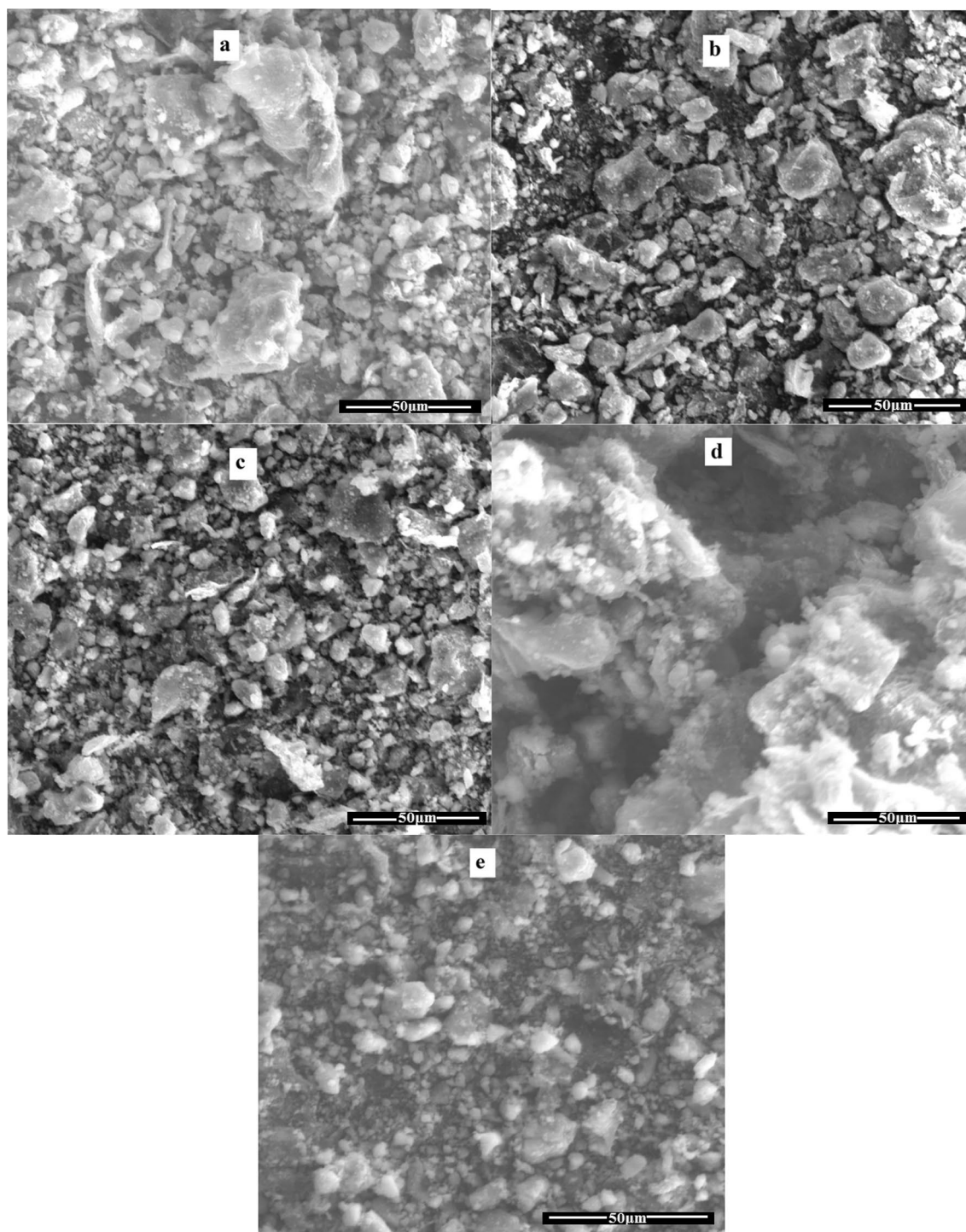


Figure 4 The SEM images of the prepared nanocatalyst, ZnFe₂O₄ NPs (a), Zn_{0.2}Cu_{0.8}Fe₂O₄ NPs (b), Zn_{0.5}Cu_{0.5}Fe₂O₄ NPs (c), Zn_{0.8}Cu_{0.2}Fe₂O₄ NPs (d) and CuFe₂O₄ NPs (e).

change. This leads to shifts in the position and intensity of the peaks in the FTIR spectrum. The magnitude of the shift depends on the specific vibrational mode and the amount of Zn and Cu present. Zn and

Cu have different electronic configurations, which can affect the electronic transitions in the material. This can lead to changes in the intensity of the FTIR bands, even if the vibrational frequencies remain the same

Table 1 EDX elemental analysis of the prepared $Zn_xCu_{(1-x)}Fe_2O_4$ nanoparticles

	Element							
	Zn		Cu		Fe		O	
	wt%	at%	wt%	at%	wt%	at%	wt%	at%
$CuFe_2O_4$	0	0	34.58	15.8	40.64	26.4	24.78	54.47
$Cu_{0.8}Zn_{0.2}Fe_2O_4$	8.22	4.38	24.5	13.55	41.44	25.8	25.84	56.27
$Cu_{0.5}Zn_{0.5}Fe_2O_4$	16.74	9.48	16.88	9.83	44.12	29.23	22.26	51.47
$Cu_{0.2}Zn_{0.8}Fe_2O_4$	25.28	13.95	7.28	4.25	43.74	28.3	23.7	53.5
$ZnFe_2O_4$	34.62	15.6	0	0	40.91	25.8	24.4	56.2

[41]. Overall, the effects of Zn/Cu ratios on FTIR transmittance bands are complex and depend on several factors.

Photocatalytic potential of $Zn_xCu_{(1-x)}Fe_2O_4$ nanoparticles on MO.

In this part of the work, the photocatalytic potential of the synthetic ferrite $Zn_xCu_{(1-x)}Fe_2O_4$ nanoparticles was explored to methyl orange dye under the radiation of UV lamp.

A UV–Vis DR5000 spectrophotometer operating at a wavelength of 464 nm was used to measure the concentration of the (MO) dye as indicated in Fig. 7a [42]. Figure 7b shows the calibration curve of (MO) at different concentrations (5, 10, 15, 20, 30 ppm).

The experiments were carried out with fixed concentrations of MO and $Zn_xCu_{(1-x)}Fe_2O_4$ nanoparticles. The optimum composition for $Zn_xCu_{(1-x)}Fe_2O_4$ nanoparticles corresponding to certain x values was selected for further analysis of different parameters. From the screening results, we can expect that $Zn_{0.5}Cu_{0.5}Fe_2O_4$ NPs have higher efficiency for the removal of MO as represented in Fig. 8a.

Different UV irradiation protocols are illustrated in the references. Some recommend delayed UV irradiation by 30 min or more to eliminate the adsorption effect [43]. On the other hand, many authors recommend the methyl orange (MO) inaction of UV irradiation and adsorption without any delay [44]. In this part of the work, a comparative test was employed to determine the significance of delayed irradiation or starting the UV irradiation from zero time. Figure 8b shows that the degradation of MO dye due to photolysis after 135 min was only 6.0%; the photolysis of MO was insignificant because the $OH\cdot$ and $H\cdot$ radicals it produced were ineffective in UV-oxidation processes in the absence of an appropriate catalyst [45]. On the other hand, the removal due to adsorption in the

dark was around 29.0% after the same amount of time, as shown in Fig. 8b. The dye degradation percentage after photocatalytic treatment with $Zn_{0.5}Cu_{0.5}Fe_2O_4$ NPs nanoparticles was measured to be 71.0. These results indicate that the higher surface to volume ratio of $Zn_{0.5}Cu_{0.5}Fe_2O_4$ NPs nanoparticles helps to accommodate a higher degree of dye molecular adsorption on their surface, and leads to degradation upon UV light excitation.

Effect of pH

A fundamental factor in removal findings is the reliance on the solution's pH level. For 135 min, following a set of experimental circumstances (10 mg prepared nanoparticles, 50 ml of 10 ppm methyl orange (MO) solution, and a temperature of 25 °C), the effects of the beginning pH of the solution were examined. Figure 9a displays a plot of the variance in methyl orange (MO) removal (%) over time at various solution pHs (3.0, 5.0, 7.0, and 9.0). At pH 3.0, the greatest percentage of methyl orange (MO) removal was seen during equilibrium. 10 mg of $Zn_{0.5}Cu_{0.5}Fe_2O_4$ NPs was put into 50 mL of 0.01 M NaCl solution to obtain the point of zero charge (PZC) of the $Zn_{0.5}Cu_{0.5}Fe_2O_4$ NPs. The solutions' pH levels were changed to 2, 4, 6, 8, 10, 12 by applying HCl or NaOH. The samples were agitated at 200 rpm for 48 h. After ($Zn_{0.5}Cu_{0.5}Fe_2O_4$ NPs) were separated magnetically, the pH of the solutions was assessed.

A plot relating the initial and final pH was used to determine the pH of the PZC value. Figure 9b displays these findings. The pH of the PZC was found to be 6.7, as shown in Fig. 9a, with no discernible difference between the end and beginning pH readings. The photocatalyst ($Zn_{0.5}Cu_{0.5}Fe_2O_4$ NPs) has a positive and negative surface charge depending on the pH and PZC. Additionally, once the pH of the solution is equal to the pH of the PZC, the charge of the area of the photocatalyst surface is neutral and the electrostatic force between the

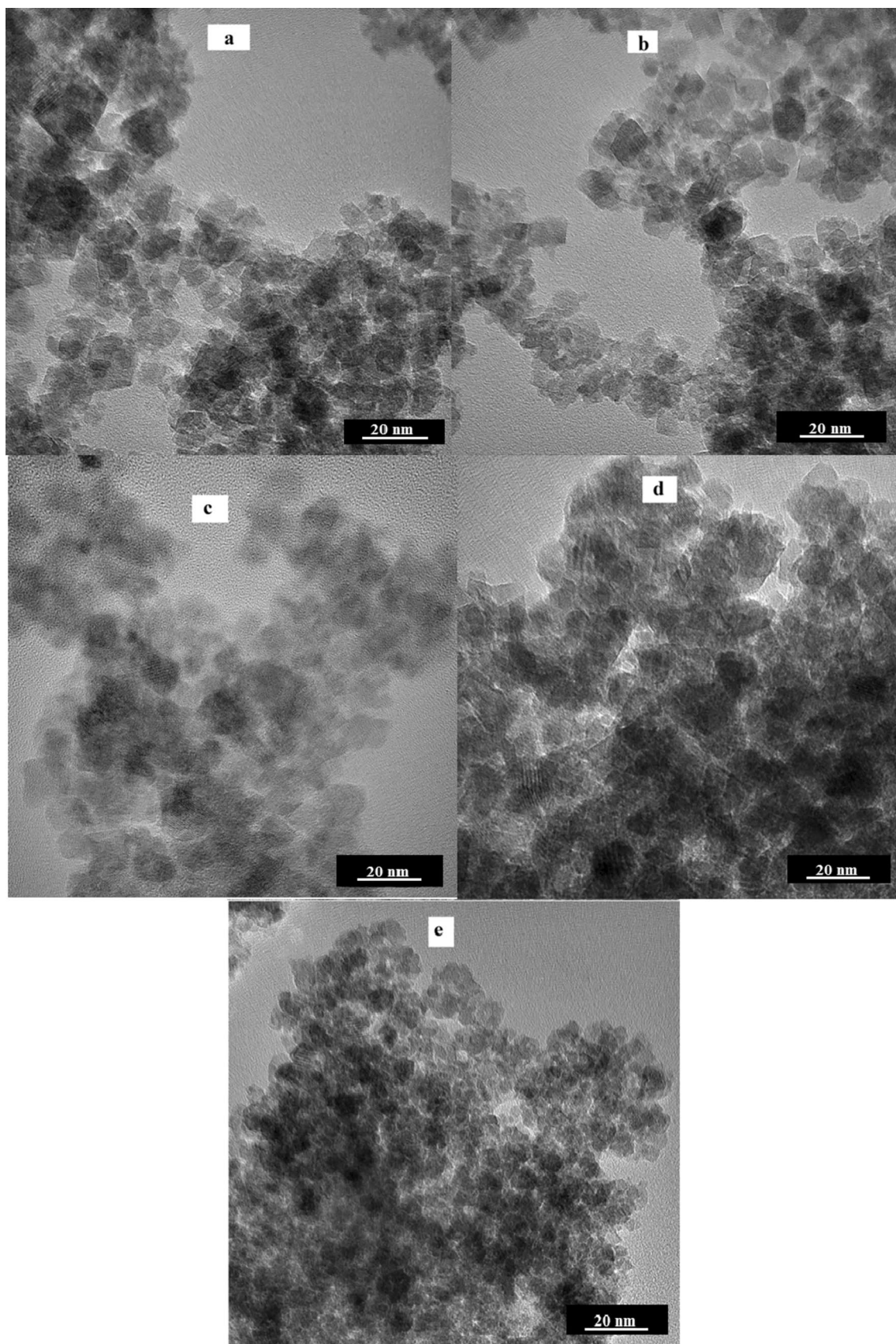


Figure 5 TEM imageries of the produced nanocatalyst, ZnFe₂O₄ NPs (a), Zn_{0.2}Cu_{0.8}Fe₂O₄ NPs (b), Zn_{0.5}Cu_{0.5}Fe₂O₄ NPs (c), Zn_{0.8}Cu_{0.2}Fe₂O₄ NPs (d) and CuFe₂O₄ NPs (e).

photocatalyst surface and ions (methyl orange (MO) ions) is insignificant [46]. The photocatalytic degradation of methyl orange (MO) was maximal at pH 3.0 as shown in Fig. 9a, and this result was verified by the pH of the PZC value, which indicated that the pH of the PZC-related Zn_{0.5}Cu_{0.5}Fe₂O₄ was 6.7. As a result, the photocatalytic degradation of methyl orange (MO) is improved at this stage because the Zn_{0.5}Cu_{0.5}Fe₂O₄ NPs' net surface charge is positive and attracts the negative charge of methyl orange (MO). At pH 9.0, the photocatalytic degradation of methyl orange (MO) began to slow down. This is because, at this pH, the Zn_{0.5}Cu_{0.5}Fe₂O₄ NPs' net surface charges are negative, creating the repulsion force between the negative charges of methyl orange (MO) and the Zn_{0.5}Cu_{0.5}Fe₂O₄ nanocomposite. The unexpected decrease in photocatalytic degradation at pH 5.0 is caused by the possibility of metal oxide leaching in extremely acidic media, which lowers the catalyst concentration [47].

Effect of the initial concentration

Due to the significance of the beginning MO concentration in the removal procedure, the effect of MO ionic strength was investigated by varying the beginning MO concentration while keeping the further reaction settings constant. Different beginning MO concentrations (5.0, 10.0, and 15.0 ppm) are shown in Fig. 10a along with the progression in removal percentage as a function of contact time. According to the findings, MO, which can be efficiently eliminated in the presence of the synthesized Zn_{0.5}Cu_{0.5}Fe₂O₄ nanocatalyst below UV light irradiation with high beginning concentrations, is degraded with an efficiency that is inversely proportional to MO concentration.

Effect of the nanocomposite dose on degradation efficiency.

By adjusting the amount of the prepared photocatalyst between 5 and 15 mg alongside a set concentration of MO 10 ppm, as shown in Fig. 10b, it was possible to determine the influence of a nanocomposite dose on the elimination rate of MO underneath UV light. The outcomes showed that after the photocatalyst dose was amplified from (5 to

15 mg), the removal efficiency grew. The expansion in the available active area of the photocatalyst to volume ratio of the MO solution may be the cause of the detected rise in removal effectiveness with growing the amount of the photocatalyst in the reaction [48].

Kinetic studies

The degradation of MO can be calculated using the following equation:

$$-\ln C_t/C_0 = -kt \quad (3)$$

where t is the removal time, k is the removal rate constant, and (C_t and C_0) are the consequent beginning and ending concentrations of MO.

The results show that the specific mechanism by which ZnCuFe₂O₄ nanoparticles photocatalyzed MO degradation obeyed pseudo-first-order rate laws, as shown in the results presented in Fig. 11a. This indicates that the rate of MO degradation is proportional to the concentration of MO remaining in the solution. In addition, it can be observed that the value of the reaction rate constant, k , decreases in line with an increase in the initial concentration of MO, as shown in Fig. 11b, which is in a good agreement with the degradation performance results.

Besides, photocatalysts typically have a large pool of active species (e.g., photogenerated electrons, holes, or surface-bound radicals) that are constantly being regenerated by light, this ensures a steady supply of active species for reaction with the pollutant, maintaining a constant rate and pseudo-first-order kinetics [49, 50]. Photocatalytic reactions often involve adsorption of the pollutant molecule onto the surface of the catalyst. This limits the number of available active sites for reaction and can lead to pseudo-first-order kinetics, especially at low pollutant concentrations [51]. Moreover, a rise in catalyst dose causes a drop in the evident pseudo-first-order rate constants, as seen in Fig. 11b. This reliance on methyl orange (MO) concentration-dependent reaction speed constants is supportive of published studies [52].

Mechanism of photocatalysis of methyl orange (MO)

The probable process is as follows, as stated in numerous literary analyses [53–55]: explicit oxidation attributed to the positively charged holes in the valence band, explicit reduction attributed to the electrons found in the conduction band, and hydroxyl radical assault are three photo-degradation processes that are impacted by pH changes.

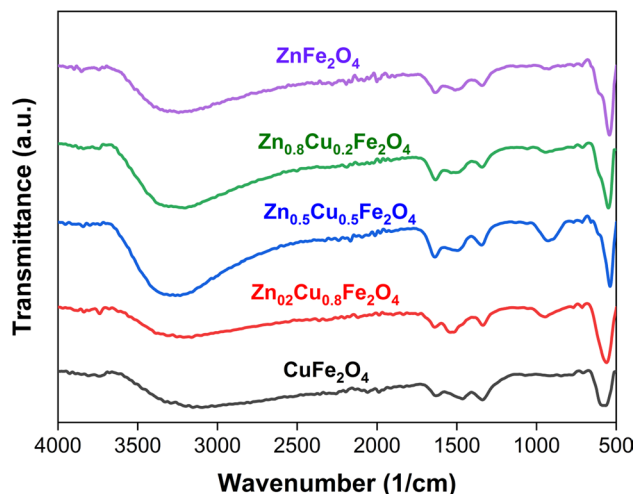
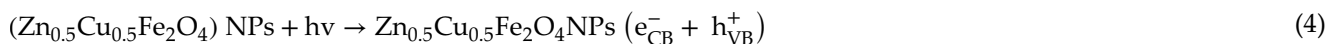
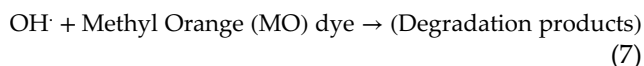


Figure 6 FTIR of the synthesized $Zn_xCu_{(1-x)}Fe_2O_4$ nanoparticles.

Because UV irradiation causes electron–hole pairs to form on the employed photocatalyst’s surface area, it is anticipated that photocatalytic elimination will take place alongside a $Zn_{0.5}Cu_{0.5}Fe_2O_4$ photocatalyst. The reactive methyl orange (MO) is oxidized by the holes’ oxidative potential to produce breakdown products or interacts with the OH groups to produce hydroxyl radicals [56]. The following table lists the reactions between the chosen photocatalyst and methyl orange (MO) (Eqs. 4–7).



or



The suggested process of interacting the synthesized nanocomposite with MO is shown in Fig. 12. When UV light has activated the $Zn_{0.5}Cu_{0.5}Fe_2O_4$ NPs, the redox processes will begin. MO will then be decomposed into minor organic compounds by the prepared free radicals like OH and O_2^\cdot . Additional findings utilizing gas chromatography–mass spectrometry (GC–MS) and high-performance liquid chromatography (HPLC) are required to further analyze the degradation products of MO, as there are no current reported publications about the degradation of MO dye.

Conclusion

In summary, $(Zn_xCu_{(1-x)}Fe_2O_4)$ nanoparticles ($x = 0, 0.2, 0.5, 0.8, 1.0$) were successfully prepared via a coprecipitation technique and characterized using optical and structural tools. Based on XRD, TEM, and SEM analyses, it is found that $(Zn_xCu_{(1-x)}Fe_2O_4)$ nanoparticles

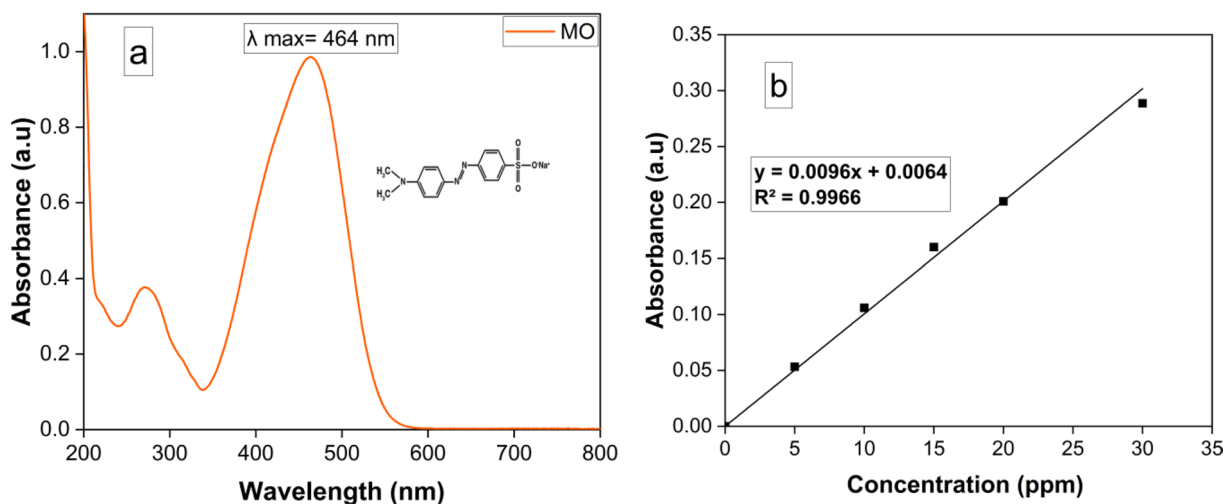


Figure 7 Methyl orange (MO) (a) UV spectrum (b) calibration curve of MO.

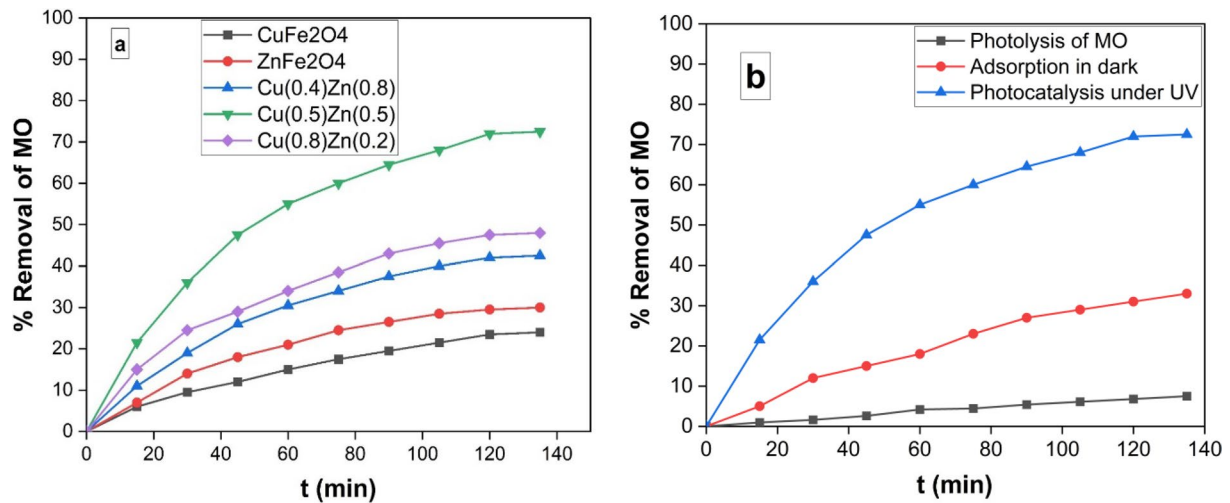


Figure 8 a The photocatalysis removal profile of 10 ppm in 50 ml MO by 10 mg of $Zn_xCu_{(1-x)}Fe_2O_4$ nanoparticles ($x=0, 0.2, 0.5, 0.8, 1$) at pH7 and ambient temperature 25 °C b shows the

stability of (MO) contaminant at concentration 10 ppm in water (hydrolysis) and under the UV radiation (photolysis) for 135 min.

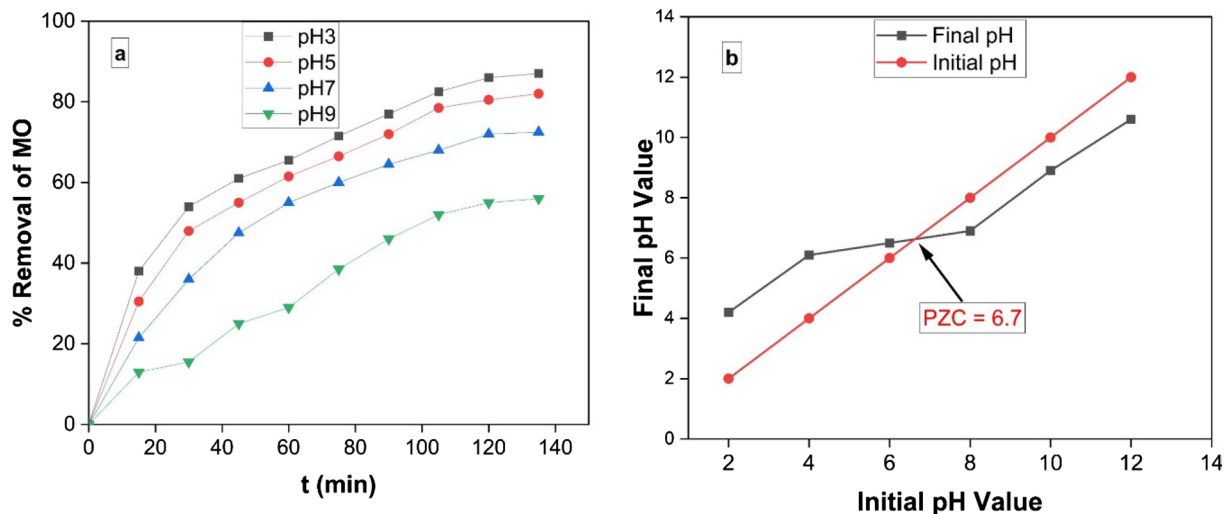


Figure 9 a Presentation of methyl orange (MO) removal (%) variation with time at various solution pH (3.0, 5.0, 7.0, and 9.0) (10 mg g of $Zn_{0.5}Cu_{0.5}Fe_2O_4$ in 50 ml of 10 ppm methyl orange (MO) at 25 °C), and b showing the PZC of $Zn_{0.5}Cu_{0.5}Fe_2O_4$.

were produced with particle sizes varying from 28.0 to 38.0 nm with average particle size at 35 nm. From FTIR results, the obtained spectra may be divided into two main regions. The first one represents the fingerprint region ($500\text{--}1800\text{ cm}^{-1}$) and the other is the lattice

water H–O–H stretching band ($3200\text{--}3600\text{ cm}^{-1}$). From the screening results of photocatalytic degradation of MO using ($Zn_xCu_{(1-x)}Fe_2O_4$), we can expect that $Zn_{0.5}Cu_{0.5}Fe_2O_4$ NPs have higher efficiency for removal of MO. Also, $Zn_{0.5}Cu_{0.5}Fe_2O_4$ NPs achieved a significant

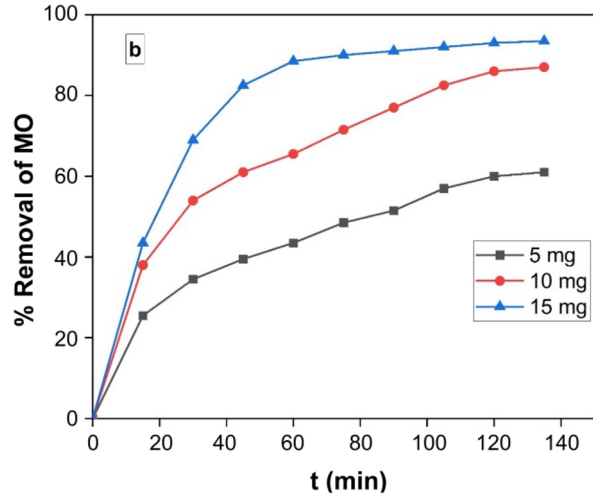
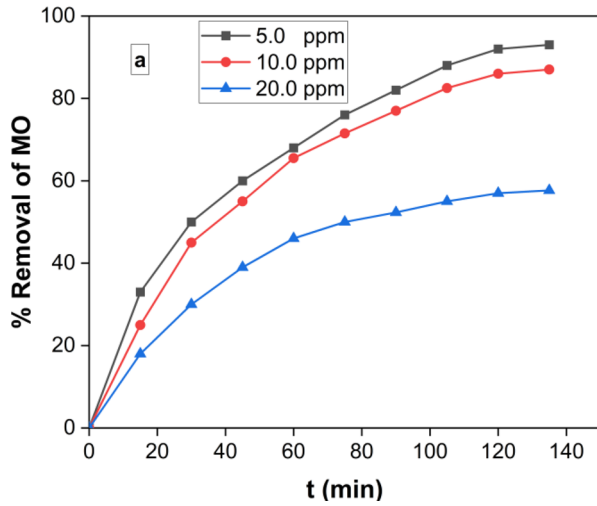


Figure 10 a The different % removal as a function of contact time at various beginning methyl orange (MO) concentrations (5.0, 10.0 and 15.0 ppm) at pH 3.0 and 10.0 mg $Zn_{0.5}Cu_{0.5}Fe_2O_4$,

and **b** effect of the photocatalyst dose on the removal efficiency of methyl orange (MO) (50 ml methyl orange (MO) solution (10 ppm), temperature of 25 °C and pH 3).

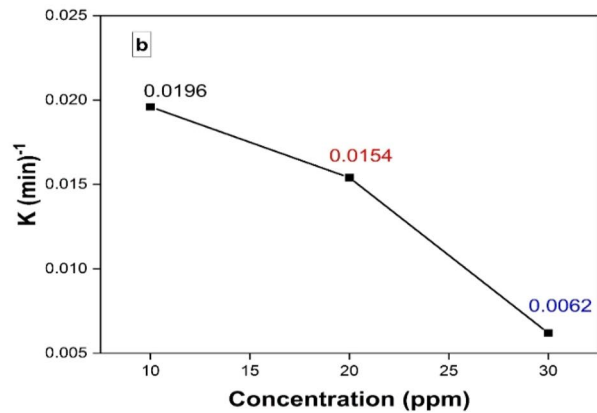
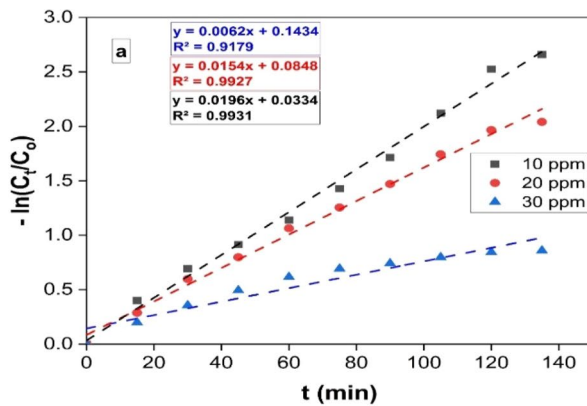


Figure 11 a Kinetics plots for data in a linear fit from a pseudo-first-order result system for the deterioration of methyl orange (MO) beneath UV light irradiation, beginning concentrations of 10 ppm of methyl orange (MO), 50 mL of 5, 10, and 15 mg of

catalyst dosage, and **b** displays a relationship between evident pseudo-first-order rate constants and initial concentration of methyl orange (MO).

photodegradation potential for methyl orange (MO) in aqueous solutions. The extreme photocatalytic effectiveness succeeded in eliminating about 96% of 10 ppm MO after 135 min with 10 mg $Zn_{0.5}Cu_{0.5}Fe_2O_4$ NPs at pH3.

Finally, the synthesized $Zn_{0.5}Cu_{0.5}Fe_2O_4$ NPs are promising for potential applications in wastewater treatment from azo dyes.

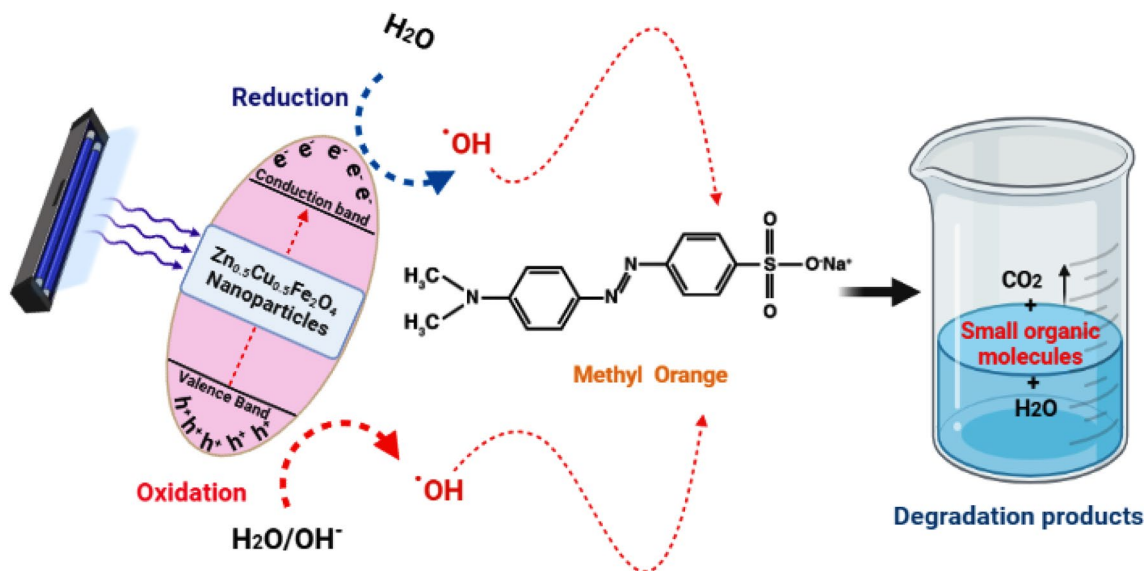


Figure 12 The potential photocatalytic reaction system for MO photodegradation via $Zn_{0.5}Cu_{0.5}Fe_2O_4$ NPs nanocomposite.

Acknowledgements

The authors express their sincere thanks to Military Technical College, Cairo, Egypt, and Galala University, Suez, Egypt, for providing the necessary research facilities.

Funding

Open access funding provided by The Science, Technology & Innovation Funding Authority (STDF) in cooperation with The Egyptian Knowledge Bank (EKB). Not applicable.

Availability of data and materials

The data used to support the findings of this study are available from the corresponding author upon request.

Declarations

Competing interests The authors declare no competing interests.

Ethics approval Not applicable.

Open Access This article is licensed under a Creative Commons Attribution 4.0 International License, which permits use, sharing, adaptation, distribution

and reproduction in any medium or format, as long as you give appropriate credit to the original author(s) and the source, provide a link to the Creative Commons licence, and indicate if changes were made. The images or other third party material in this article are included in the article's Creative Commons licence, unless indicated otherwise in a credit line to the material. If material is not included in the article's Creative Commons licence and your intended use is not permitted by statutory regulation or exceeds the permitted use, you will need to obtain permission directly from the copyright holder. To view a copy of this licence, visit <http://creativecommons.org/licenses/by/4.0/>.

References

- [1] Amiri M, Salavati-Niasari M, Akbari A (2019) Magnetic nanocarriers: evolution of spinel ferrites for medical applications. *Adv Coll Interface Sci* 265:29–44
- [2] Hakeem A et al (2021) Magnetic, dielectric and structural properties of spinel ferrites synthesized by sol–gel method. *J Mater Res Technol* 11:158–169
- [3] Cardoso VF et al (2018) Advances in magnetic nanoparticles for biomedical applications. *Adv Healthc Mater* 7(5):1700845
- [4] Vinosha PA et al (2017) Study on cobalt ferrite nanoparticles synthesized by co-precipitation technique for photofenton application. *Mech Mater Sci Eng J* 9(1):110–115

- [5] Sharifianjazi F et al (2020) Magnetic CoFe_2O_4 nanoparticles doped with metal ions: a review. *Ceram Int* 46(11):18391–18412
- [6] Jamkhande PG et al (2019) Metal nanoparticles synthesis: an overview on methods of preparation, advantages and disadvantages, and applications. *J Drug Deliv Sci Technol* 53:101174
- [7] Abuzeyad OH et al (2023) An evaluation of the improved catalytic performance of rGO/GO-hybrid-nanomaterials in photocatalytic degradation and antibacterial activity processes for wastewater treatment: a review. *J Mol Struct* 1288:135787
- [8] Boudjemaa A et al (2016) M-substituted (M = Co, Ni and Cu) zinc ferrite photo-catalysts for hydrogen production by water photo-reduction. *Int J Hydrogen Energy* 41(26):11108–11118
- [9] Yang H et al (2004) Synthesis of ZnFe_2O_4 nanocrystallites by mechanochemical reaction. *J Phys Chem Solids* 65(7):1329–1332
- [10] Xu H et al (2012) A comparative study of nanoparticles and nanospheres ZnFe_2O_4 as anode material for lithium ion batteries. *Int J Electrochem Sci* 7(9):7976–7983
- [11] Rajput N (2015) Methods of preparation of nanoparticles-a review. *Int J Adv Eng Technol* 7(6):1806–1811
- [12] El-Batal AI et al (2022) Antimicrobial synergism and antibiofilm activity of amoxicillin loaded citric acid-magnesium ferrite nanocomposite: effect of UV-illumination, and membrane leakage reaction mechanism. *Micro Patho* 164:105440
- [13] Zhang S et al (2021) Non-biodegradable microplastics in soils: a brief review and challenge. *J Hazard Mater* 409:124525
- [14] Gupta NK et al (2020) Photocatalytic degradation of organic pollutants over MFe_2O_4 (M = Co, Ni, Cu, Zn) nanoparticles at neutral pH. *Sci Rep* 10(1):4942
- [15] Ezekiel IP (2014) Structure and bi-magnetism of nanocomposites and nanoalloys synthesized by reduction of (Co, Ni) Fe_2O_4 nano-ferrites
- [16] Solomon R et al (2012) Enhanced photocatalytic degradation of azo dyes using nano Fe_3O_4 . *J Iran Chem Soc* 9:101–109
- [17] Ljubas D, Smoljanić G, Juretić H (2015) Degradation of Methyl Orange and Congo Red dyes by using TiO_2 nanoparticles activated by the solar and the solar-like radiation. *J Environ Manag* 161:83–91
- [18] Punyasamudram S et al (2023) Biosynthesis of ZnFe_2O_4 @Ag hybrid nanocomposites for degradation of 2, 4-dichlorophenoxyacetic acid herbicide. *Chem Phys Impact* 7:100282
- [19] Srinivas M (2020) Enhanced photocatalytic activity of Ag-Co Fe_2O_4 over $\text{Ni}_x\text{Co}_{1-x}\text{Fe}_2\text{O}_4$ catalyst under visible light: a comparative study. *Mater Today Proc* 22:1885–1892
- [20] Alzoubi GM et al (2020) Coexistence of superparamagnetism and spin-glass like behavior in zinc-substituted cobalt ferrite nanoparticles. *Appl Phys A* 126(7):512
- [21] Adeela N et al (2015) Influence of manganese substitution on structural and magnetic properties of CoFe_2O_4 nanoparticles. *J Alloys Compd* 639:533–540
- [22] Hoong LJ (2021) Effects of sintering atmosphere on the optical, thermal and electrical properties of inkjet printed $\text{Zn}_x\text{Cu}_{(1-x)}\text{Fe}_2\text{O}_4$ thin films. *J Adv Res Fluid Mech Therm Sci* 81(2):25–35
- [23] Dhiwaha AT et al (2020) Microwave-assisted combustion synthesis of pure and zinc-doped copper ferrite nanoparticles: structural, morphological, optical, vibrational, and magnetic behavior. *J Phys Chem Solids* 138:109257
- [24] Sarkar BJ et al (2023) Microstructural investigation of sonochemically synthesized Zn substituted CuFe_2O_4 nanoparticles for heterogeneous green catalytic click chemistry and dye degradation. *J Mol Struct* 1274:134493
- [25] Gholizadeh A (2018) A comparative study of the physical properties of Cu–Zn ferrites annealed under different atmospheres and temperatures: magnetic enhancement of $\text{Cu}_{0.5}\text{Zn}_{0.5}\text{Fe}_2\text{O}_4$ nanoparticles by a reducing atmosphere. *J Magn Magn Mater* 452:389–397
- [26] Najmoddin N et al (2014) XRD cation distribution and magnetic properties of mesoporous Zn-substituted CuFe_2O_4 . *Ceram Int* 40(2):3619–3625
- [27] Singh S, Goswami N (2022) Tailoring magnetic properties through variation of cations distribution in Zn–Cu ferrite nanoparticles prepared by exploding wire technique. *Mater Sci Eng B* 278:115608
- [28] Varshney D, Verma K, Kumar A (2011) Structural and vibrational properties of $\text{Zn}_x\text{Mn}_{1-x}\text{Fe}_2\text{O}_4$ ($x=0.0, 0.25, 0.50, 0.75, 1.0$) mixed ferrites. *Mater Chem Phys* 131(1):413–419
- [29] Najmoddin N et al (2014) Magnetic properties of crystalline mesoporous Zn-substituted copper ferrite synthesized under nanoconfinement in silica matrix. *Microporous Mesoporous Mater* 190:346–355
- [30] Manikandan A et al (2013) Structural, optical and magnetic properties of $\text{Zn}_{1-x}\text{Cu}_x\text{Fe}_2\text{O}_4$ nanoparticles prepared by microwave combustion method. *J Mol Struct* 1035:332–340
- [31] Inkson BJ (2016) 2-Scanning electron microscopy (SEM) and transmission electron microscopy (TEM) for materials characterization. In: Hübschen G et al (eds) *Materials characterization using nondestructive evaluation (NDE) methods*. Woodhead Publishing, London, pp 17–43
- [32] Schulz H (2008) Spectroscopic. In: *Modern techniques for food authentication*, p 149

- [33] Razmara Z, Janczak J (2021) Sonochemical synthesis and structural characterization of a new three mono-nuclear cobalt (II) complex, to produce tricobalt tetroxide as an effective heterojunction catalyst. *J Mol Struct* 1229:129500
- [34] Shahzad K et al (2022) Silver supported-Ag@ PMOS onto thumb structured porous organosilica materials with efficient hetero-junction active sites for photo-degradation of methyl orange dye. *Inorg Nano-Metal Chem* 52(3):407–416
- [35] Ishfaq M et al (2023) Synthesis of binary metal doped CeO₂ via the subcritical hydrothermal method for photo-mineralizing methyl orange dye. *J Alloys Compd* 960:170661
- [36] Jaskot MB (2020) Linking morphology to electronic properties in small-molecular organic semiconductors
- [37] Lassoued A et al (2018) Retracted article: photocatalytic degradation of methyl orange dye by NiFe₂O₄ nanoparticles under visible irradiation: effect of varying the synthesis temperature. *J Mater Sci Mater Electron* 29:7057–7067
- [38] Wang J et al (2022) Multifunctional core-double-shell C@ MnO@ TiO₂ catalysts with enhanced full-light conversion for the highly efficient photothermal oxidation of toluene. *Appl Catal B* 317:121789
- [39] Yilmaz MS (2022) Graphene oxide/hollow mesoporous silica composite for selective adsorption of methylene blue. *Microporous Mesoporous Mater* 330:111570
- [40] Gawade VV et al (2017) Green synthesis of ZnO nanoparticles by using *Calotropis procera* leaves for the photo-degradation of methyl orange. *J Mater Sci Mater Electron* 28:14033–14039
- [41] Zaki HM, Dawoud HA (2010) Far-infrared spectra for copper–zinc mixed ferrites. *Physica B* 405(21):4476–4479
- [42] Pérez-Ramírez EE et al (2019) One- and two-dimensional carbon nanomaterials as adsorbents of cationic and anionic dyes from aqueous solutions. *Carbon Lett* 29:155–166
- [43] Huang Y et al (2014) Oxygen vacancy induced bismuth oxyiodide with remarkably increased visible-light absorption and superior photocatalytic performance. *ACS Appl Mater Interfaces* 6(24):22920–22927
- [44] Kite SV et al (2021) Nanostructured TiO₂ sensitized with MoS₂ nanoflowers for enhanced photodegradation efficiency toward methyl orange. *ACS Omega* 6(26):17071–17085
- [45] Anisuzzaman SM et al (2022) Current trends in the utilization of photolysis and photocatalysis treatment processes for the remediation of dye wastewater: a short review. *ChemEngineering* 6(4):58
- [46] Aminuddin NF, Nawi MA, Bahrudin NN (2022) Enhancing the optical properties of immobilized TiO₂/polyaniline bilayer photocatalyst for methyl orange decolorization. *React Funct Polym* 174:105248
- [47] Venkatachalam N, Palanichamy M, Murugesan V (2007) Sol–gel preparation and characterization of alkaline earth metal doped nano TiO₂: efficient photocatalytic degradation of 4-chlorophenol. *J Mol Catal A Chem* 273(1–2):177–185
- [48] Verma S et al (2019) Studies on growth of Au cube-ZnO core-shell nanoparticles for photocatalytic degradation of methylene blue and methyl orange dyes in aqueous media and in presence of different scavengers. *J Environ Chem Eng* 7(4):103209
- [49] Rangarajan G, Jayaseelan A, Farnood R (2022) Photocatalytic reactive oxygen species generation and their mechanisms of action in pollutant removal with biochar supported photocatalysts: a review. *J Clean Prod* 346:131155
- [50] Wang JL, Xu LJ (2012) Advanced oxidation processes for wastewater treatment: formation of hydroxyl radical and application. *Crit Rev Environ Sci Technol* 42(3):251–325
- [51] Konstantinou IK, Albanis TA (2004) TiO₂-assisted photocatalytic degradation of azo dyes in aqueous solution: kinetic and mechanistic investigations: a review. *Appl Catal B* 49(1):1–14
- [52] Al-Odayni A-B, Alsubaie FS, Saeed WS (2023) Nitrogen-rich polyaniline-based activated carbon for water treatment: adsorption kinetics of anionic dye methyl orange. *Polymers* 15(4):806
- [53] Yu L et al (2012) The degradation mechanism of methyl orange under photo-catalysis of TiO₂. *Phys Chem Chem Phys* 14(10):3589–3595
- [54] El-Khawaga AM et al (2022) Synthesis and applicability of reduced graphene oxide/porphyrin nanocomposite as photocatalyst for waste water treatment and medical applications. *Sci Rep* 12(1):17075
- [55] El-Khawaga AM et al (2023) Promising photocatalytic and antimicrobial activity of novel capsaicin coated cobalt ferrite nanocatalyst. *Sci Rep* 13(1):5353
- [56] Zhang Z et al (2020) Degradation of methyl orange through hydroxyl radical generated by optically excited biochar: performance and mechanism. *Colloids Surf A* 601:125034

Publisher's Note Springer Nature remains neutral with regard to jurisdictional claims in published maps and institutional affiliations.